Magnetic Direct-Write Skyrmion Nanolithography

A.V. Ognev[1], A.G. Kolesnikov[1], Yong Jin Kim[2], In Ho Cha[2], A.V. Sadovnikov[3,4], S.A. Nikitov[3,4], I.V. Soldatov[5,10], A. Talapatra[6], J. Mohanty[6], M. Mruczkiewicz[7,11], Y. Ge[8], N. Kerber[8], F. Dittrich[8], P. Virnau[8], M. Kläui[8], Young Keun Kim[2*], A.S. Samardak[1,9**]

[1]School of Natural Sciences, Far Eastern Federal University, Vladivostok 690950, Russia

[2]Department of Materials Science and Engineering, Korea University, Seoul 02841, Republic of Korea

[3]Laboratory "Metamaterials", Saratov State University, Saratov 410012, Russia

[4]Kotel'nikov Institute of Radioengineering and Electronics, Russian Academy of Sciences, Moscow 125009, Russia

[5]Leibniz Institute for Solid State and Material Research (IFW-Dresden), Dresden 01069, Germany

[6]Indian Institute of Technology, Hyderabad 502285, India

[7]Institute of Electrical Engineering, SAS, Bratislava 841 04, Slovakia

[8]Institut für Physik, Johannes Gutenberg-Universität Mainz, Mainz 55128, Germany

[9]National Research South Ural State University, Chelyabinsk 454080, Russia

[10]Institute of Natural Sciences and Mathematic, Ural Federal University, Yekaterinburg 620075, Russia

[11]Centre for Advanced Materials Application (CEMEA), Slovak Academy of Sciences, Bratislava 845 11, Slovakia

Abstract

Magnetic skyrmions are stable spin textures with quasi-particle behavior and attract significant interest in fundamental and applied physics. The meta-stability of magnetic skyrmions at zero magnetic field is particularly important to enable, for instance, a skyrmion racetrack memory. Here, the results of the nucleation of stable skyrmions and formation of ordered skyrmion lattices by magnetic force microscopy in $(Pt/CoFeSiB/W)_n$ multilayers, exploiting the additive effect of the interfacial Dzyaloshinskii–Moriya interaction, are presented. The appropriate conditions under which confined skyrmion lattices with a dense two-dimensional liquid phase are identified. A crucial parameter to control the skyrmion lattice characteristics and the number of scans resulting in the complete formation of a skyrmion lattice is the distance between two adjacent scanning lines of a magnetic force microscopy probe. The creation of skyrmion patterns with complex geometry is demonstrated, and the physical mechanism of direct magnetic writing of skyrmions is comprehended by micromagnetic simulations. This study shows a potential of a direct-write (maskless) skyrmion (topological) nanolithography with sub-100 nm resolution, where each skyrmion acts as a pixel in the final topological image.

Keywords: skyrmion, interfacial Dzyaloshinskii–Moriya interaction, perpendicular magnetic lithography, magnetic force microscopy, topological nanolithography

Despite the explosive interest in nontrivial spin textures,[1–3] numerous challenges in skyrmion stabilization[4] remain unresolved. Particularly, skyrmion lattices[5] are promising for racetrack memory,[6,7] non-conventional logic,[8] and neuromorphic computing.[9,10] As exhibited earlier for an ultrathin ferromagnetic film (FM) with perpendicular magnetic anisotropy (PMA), placed between two *4d* or *5d* heavy metals (HM_1 and HM_2 with opposite signs of the interfacial Dzyaloshinskii–Moriya interaction (IDMI)),[11] isolated skyrmions are observed only in an applied magnetic field, which compensates the lack of the IDMI energy competing with PMA and direct exchange.[12–14] In particular cases, skyrmions can be generated by the application of a certain sequence of tilted external fields; however, in a zero field, the size and spatial distribution of skyrmions are strongly inhomogeneous.[15] The external magnetic field can be replaced by interlayer exchange coupling, which is an effective magnetic field oriented normal to the film plane, thereby stabilizing the skyrmion lattice in zero field.[16,17] To reduce the effect of the magnetic anisotropy energy, multilayer structures of $(HM_1/FM/HM_2)_n$ type can be used, where n is the number of repetitions of a three-layer stack. In such a system, the magneto-static interactions between the layers assist in stabilizing both skyrmions[18,19] and skyrmion lattices,[20,21] primarily in ferrimagnetic multilayers with numerous repetitions of stacks.[22,23] Recently, it has been proposed to use local stray fields of a magnetic force microscopy (MFM) probe,[24-28] an electric field,[29] radiofrequency (RF) excitations,[18] femtosecond laser pulses,[30] a focused electron beam[31] and heating by current pulses[32] for the nucleation of isolated skyrmions and skyrmion lattices.

Zhang *et al.*[24] presented a general concept of skyrmion nucleation by the stray field of a MFM tip and demonstrated a reliable approach for the skyrmion lattice formation based on the tip multipassing over a sample surface. The authors showed the importance of the tip's lift height and an external magnetic field for a skyrmion generation, but the scanning step (a distance between

two adjacent scanning lines), being a crucial parameter to control skyrmion lattice characteristics (size, density, ordering phase), was kept constant. Based on numerical calculations and using an analytical model, Garanin *et al.*[25] exhibited a similar approach of a direct skyrmion writing with a tiny magnetic dipole. At the same time, the formation of a labyrinth structure and individual skyrmions by a magnetic probe was demonstrated.[26] Further development of the field enabled the manipulation of individual skyrmions through the MFM-probe-induced local field gradient.[27]

In this study, the MFM tip-assisted transformation of a labyrinth domain structure into ordered skyrmion lattices with a certain skyrmion size and packing density is demonstrated. In addition to the tip's lift height and an external magnetic field, we consider operating the scanning step to manipulate the size and packing density of skyrmions, which are essential parameters for practical applications. Our approach allows decreasing the number of scans resulting in the complete formation of a skyrmion lattice after one tip pass only. Furthermore, the effect of IDMI on the MFM-tip-assisted nucleation of highly dense skyrmion lattices with the controllable lattice constant, size and chirality of skyrmions is studied experimentally and numerically. The micromagnetic simulations are used to confirm the importance of the scanning step and to demonstrate the relation between the local magnetic field spot size and the domain wall width. To assess the nature of the skyrmion lattice formation, the parameter space is ascertained to quantify the lattice ordering with help of the one-dimensional pair correlation function *g(r)* and the local orientational order parameter ψ_6.

Our approach is tested on multilayer structures with a Pt/CoFeSiB/W stack and repetitions (n) up to 21, which have PMA and the additive effect of the IDMI from the bottom HM_1/FM and top FM/HM_2 interfaces.[11] The inter-stack magnetostatic interaction in the structures with $n > 4$, along with the enhanced IDMI, results in zero net magnetization in the absence of an external field,

achieved by multidomain state formation with oppositely magnetized domains. However, even in such structures, the spontaneous nucleation of a skyrmion lattice does not occur; instead, a labyrinth domain structure with a period of approximately 150–200 nm is formed under ambient conditions.[33]

For the emergence of skyrmions, the required additional trigger can be provided by an external magnetic field if a skyrmion lattice is in the ground state with the lowest energy. We demonstrate that using a local stray field gradient of an MFM probe, the magnitude of which at the point of contact with a magnetic film can reach a few kOe, it is possible to not only nucleate Néel-type isolated skyrmions of 100–150 nm size but also to realize a hexagonally ordered skyrmion lattice with a period of 150–250 nm, which is not necessarily the lowest energy ground state. We find that the value of the scanning step and the number of passes along the X and Y axes in the tapping mode prior to the magnetic imaging define the number of skyrmions, including the skyrmion areal density.

The micromagnetic simulations reveal that skyrmion creation occurs owing to the slicing of the labyrinth or stripe domain structures by the local magnetic field induced by the tip apex. The simulations exhibit that the IDMI magnitude determines not only the skyrmion lattice constant but also the chirality of coupled skyrmions composing a skyrmion tube through the multilayers. Thus, the development of our approach for slicing skyrmions and their lattices allows us to establish an advanced method of direct-write skyrmion nanolithography. It can fabricate geometrical patterns based on the transformation of the surface magnetic topology, with a sub-100 nm resolution, for reservoir computing,[34] mobile atom traps,[35] and reconfigurable magnonic crystals.[36, 37]

Results and discussion

Samples characterization

A series of samples based on a Ta(3)/Pt(7)/[Pt(1)/CoFeSiB(1.5)/W(1)]$_n$/Ta(5) structure with number of stacks n = 1, 3, 5, 11, 21 was prepared by magnetron sputtering in ultrahigh vacuum with base pressure below 5×10^{-9} Torr. In this series, the Pt and W layers are the PMA and IDMI drivers on the bottom and top interfaces of the $Co_{70.5}Fe_{4.5}Si_{15}B_{10}$ layer (the content is in at.%), respectively. It is known that the Pt/FM interface has a negative sign of the IDMI,[12] whereas W/FM has a positive one.[13] In the Pt/FM/W structure, the additive effect of the IDMI is expected, which leads to an enhancement in the chiral properties.[11] Using Brillouin light scattering (BLS) spectroscopy, the magnitude of the effective IDMI (D_{eff}) for the multilayer Pt/CoFeSiB/W structure was found to be $D_{eff} \approx -1.09$ erg/cm^2, which is almost independent of the number of stack repetitions. With an increase in n, the magneto-static interaction between the magnetic layers is enhanced, which can be observed in the shape of magnetic hysteresis loops obtained in the out-of-plane (OOP) measurement geometry, as shown in Fig. S1(a) in the Supplementary file. In the case of a single Pt/CoFeSiB/W stack, the loop is rectangular, whereas, for the in-plane (IP) geometry, the loop is inclined and hysteresis-free (Fig. S1(b) in the Supplementary file), indicating the presence of PMA. The introduction of additional stacks strongly transforms the loop taken in the OOP geometry: the critical domain nucleation field H_n, seen as the onset of the decline in the net magnetization on the field decreasing from positive H_{sat} (negative H_s) saturation, is shifted from negative (positive) H_z field ranges for samples with n = 1 to the same field sign as that of the saturation field for samples with $n > 2$. Specifically, an increasing magneto-static coupling between the magnetic layers sandwiched between the layers of two *5d* metals with increasing n shifts H_n

towards the initial saturation field H_{sat}. The detailed description of sample fabrication and characterization is given in the Methods section.

Magnetic domain structure

Images of the domain structure, depending on the external magnetic field (H_z) applied normally to the sample plane, were obtained by full-field magnetic transmission soft X-ray microscopy (MTXM), as shown in Fig. 1. At the initial state (the sample was not exposed to external magnetic fields after deposition), a labyrinth structure with domains of 150–200 nm width is observed, as shown in Fig. 1(a). The application of a small external magnetic field leads to the formation of worm-like domains, as shown in Figs. 1(b, c). As can be seen, the spontaneous formation of skyrmions does not occur, which may correspond to the case when the IDMI energy is less than the critical energy of the skyrmion nucleation.[12, 18] To generate skyrmions and, in particular, the desired skyrmion ensembles, it is required to locally "write" the skyrmions. This can be achieved by a local magnetic field that can transform the worm-like domains into more compact chiral textures.

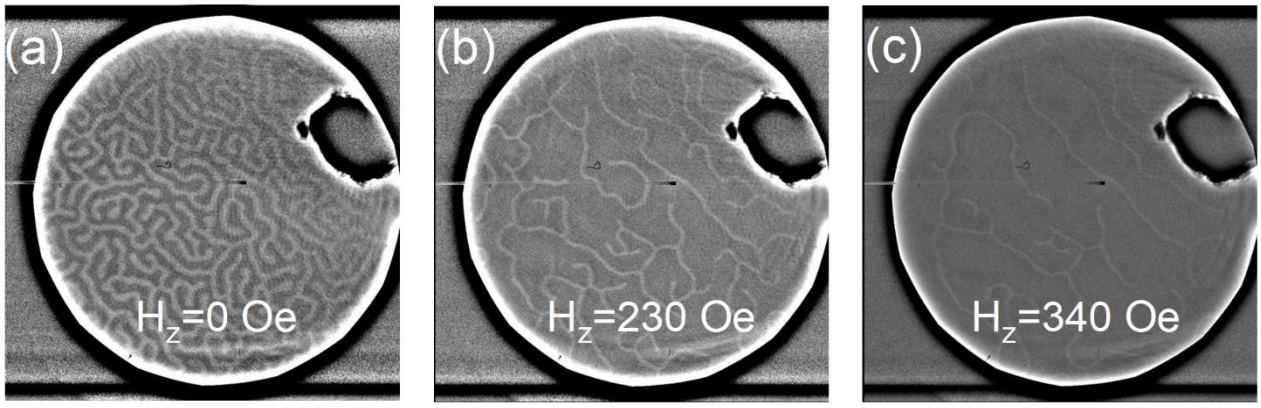

Figure 1. MTXM images of the domain structure of the $(Pt/CoFeSiB/W)_{11}$ sample captured at zero field (a), H_z = 230 Oe (b), and H_z = 340 Oe (c). The diameter of the viewing area is 10 μm.

The MFM-assisted study confirmed that in the absence of an external field, samples with $n > 5$ have a multidomain state with zero remanence, as displayed in Fig. S2(b) in the Supplementary file for the sample with $n = 11$. The domain structure is represented by alternating stripe domains with a period of 150–230 nm. However, after the second pass scanning of the sample surface with the higher resolution by the magnetic tip in the tapping and non-contact mode, the domain structure is changed (see Fig. S3(c) in the Supplementary file). The stray fields originating from the magnetic tip affect the domain structure, thus transforming the shape of the stripe domains and reducing their length. The round-shaped domains are visible between the stripe domains, which can be attributed to the skyrmions having a characteristic size of 80–100 nm. After this experiment, a detailed study on the effect of an MFM tip on the domain structure, particularly on the controllable skyrmion lattice generation, was conducted.

MFM-tip assisted skyrmion lattice nucleation

First, we checked the stability of skyrmions nucleated in the scanning process. A magnetic field $H_z = -800$ Oe, which is sufficient to saturate both the probe and sample, was applied before the scanning. The demagnetized ground state with the labyrinth domain structure was formed after switching off the external magnetic field. To enhance the effect of the negatively magnetized probe, the tapping mode scan was performed at zero field. The number of magnetic tip passes (N) in the X and Y directions was 5, whereas the scanning step, which is the distance between two adjacent scanning lines, was $s = 40$ nm.

After scanning in the tapping mode with $N = 5$, non-contact mode scanning was performed, and skyrmions and the labyrinth domain structure were observed, as shown in Fig. 2(a). The skyrmions can form a lattice with hexagonal ordering within the first coordination sphere (marked by a dashed

line in Fig. 2(a)). Subsequently, the magnetic structure was scanned only in the non-contact mode. To test the stability of the skyrmion lattice, the external magnetic field was increased up to +400 Oe (Figs. 2 (b−d)). Consequently, the diameter of skyrmions (D_{Sk}) with the positive polarity increased from 150 to 190 nm, and a few skyrmions grew and merged with each other to acquire an oblong shape.

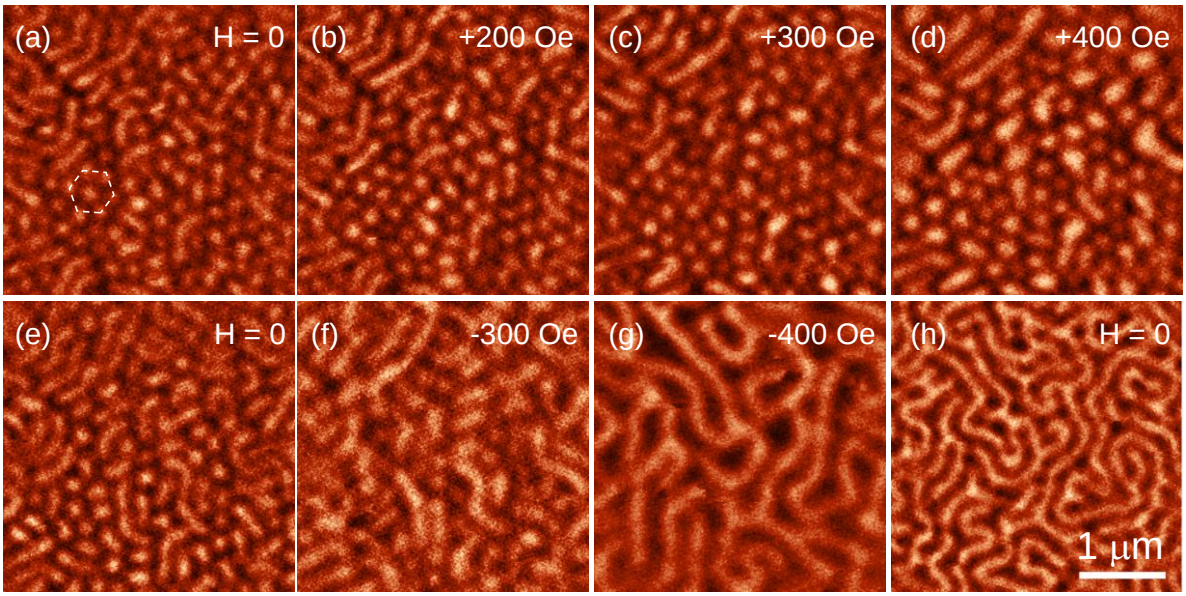

Figure 2. MFM images of the domain structure of the $(Pt/CoFeSiB/W)_{11}$ film recorded after the five-pass scanning in the tapping mode in the fields from 0 to +400 Oe (a–d), then from 0 to −400 Oe, and again in zero field (h). The dashed line in (a) marks a hexagonal unit cell of the skyrmion lattice. The bright contrast corresponds to the magnetization oriented along the positive external field and the dark one – along the negative direction.

As the magnetic field is reduced to zero, D_{Sk} decreases to 150 ± 15 nm. If the negative field of −300 Oe is applied, most of the skyrmions annihilate; in the field H_z = −400 Oe, only the labyrinth domain structure with the period P_{DS} = 290±40 nm remains. After the application of a negative saturation field H_{sat} = −700 Oe, again in zero field, the labyrinth domain structure is formed with

a smaller P_{DS} = 225 ± 40 nm, as shown in Fig. 2(h). This state is the ground state and is observed in the cases of both remnant magnetization and demagnetization by an alternating field with a decreasing amplitude. Thus, the skyrmions that are stable in a wide range of external magnetic fields can be generated by magnetic tip scanning in the tapping mode.

Without local activation by the MFM tip, only a labyrinth structure is spontaneously formed. To improve the ordering quality of the skyrmion lattice, the sample surface was scanned in the presence of an external magnetic field H_z. The following procedure was used: the field H_z was reduced from −800 to −300 Oe, and the selected area of 2.3 × 2.3 μm^2 was scanned once in the tapping mode with s = 40 nm. Then, H_z was reduced to −200 Oe, the scan area was shifted, and one-pass scan was run again in the tapping mode. The same procedure was repeated for H_z = −100 and 0 Oe. Finally, all areas were scanned in the non-contact mode. The resulting images of the magnetic structure are displayed in Fig. 3(a). With decreasing H_z, the number of generated skyrmions (N_{Sk}) decreases: in the field H_z = −300 Oe, 68 skyrmions were nucleated, whereas in zero field, N_{Sk} = 4. From the magnetic hysteresis loop of the $(Pt/CoFeSiB/W)_{11}$ structure (Fig. S1 in the Supplementary file), it follows that in the field H_z below ± 250 Oe, the magnetization drops sharply, and domains are formed. It was assumed that if the direction of the external magnetic field H_z and the stray field created by the MFM tip coincide, the effect of the tip is enhanced, and the probability of a localized skyrmion formation is increased, as experimentally observed in Fig. 3(a).

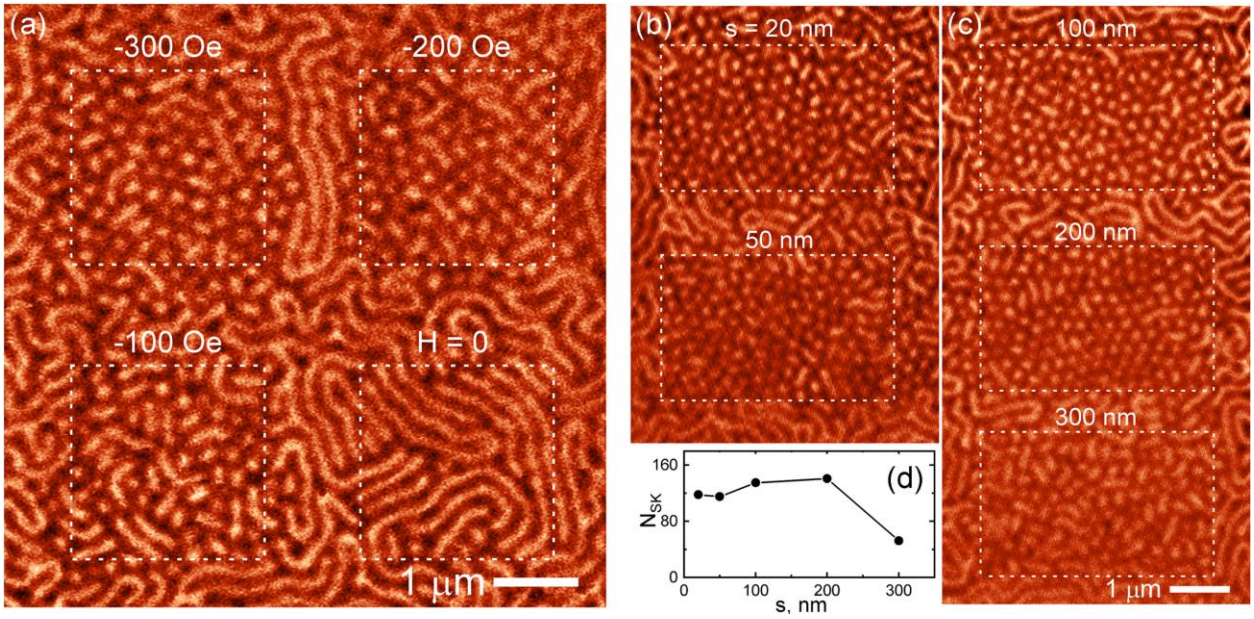

Figure 3. (a) Domain structure of the $(Pt/CoFeSiB/W)_{11}$ film with four areas (2.3×2.3 μm^2) scanned once in the tapping mode in the presence of H_z = −300, −200, −100, and 0 Oe. The MFM images of the domain structure of the $(Pt/CoFeSiB/W)_{11}$ film recorded after scanning with s = 20 and 50 nm (b), and 100, 200, and 300 nm (c). The preliminary scanning was done in the tapping mode in H_z = −300 Oe. Each scanning area was 4×2.5 μm^2. The white dashed lines delimit the scanning area in the tapping mode. (d) Dependence of N_{Sk} on s in the tapping mode.

Furthermore, the effect of the scanning step in the tapping mode on the number of nucleated skyrmions was investigated. During the scan, the tip was moved first along the X-direction and then along Y-direction. The number of scans was 5 for each direction. The scanning step sizes were s = 20, 50, 100, 200, and 300 nm. It means that the step was smaller, equal to, or larger than the skyrmion lattice period $P_{Sk} \approx 200$ nm. The scanning process in the tapping mode was performed in H_z = −300 Oe. After that, the magnetic field was turned off, and the scanning was performed in the non-contact MFM mode. The results are presented in Figs. 3(b, c). It is seen that when the scanning was performed with a small step (images for s = 20, 50, and 100 nm in Fig. 3(b)) the

magnetic structures were similar. A skyrmion lattice was formed; however, the fragments of the labyrinth structure are still presented in the form of short-length elongated domains. After scanning with a larger step, N_{Sk} increases (Fig. 3(d)). For s = 200 nm, which is close to P_{Sk}, N_{Sk} and the skyrmion lattice ordering degree are maximum. Subsequently, when s = 300 nm, *i.e.*, larger than P_{Sk}, N_{Sk} decreases sharply, and elements of the labyrinth domain structure are observed, as shown in Fig. 3(c).

Skyrmion (topological) nanolithography

To demonstrate the possibility of a controlled generation of a skyrmion lattice (topological skyrmion nanolithography), a square area of 6 × 6 μm^2 was filled with skyrmions using the optimal scan parameters described above (five-pass scanning in the tapping mode, H_z = −300 Oe, s = 200 nm). Inside this area, there was a non-scanned square area (2 × 2 μm^2) with the labyrinth domain structure remaining as displayed in Fig. 4(a). After scanning of the central square area as well, a homogeneous area with skyrmions was obtained, as shown in Fig. 4(b). As shown in Fig. 4(c), the skyrmion nanolithography can be used to create regions of complex shapes covered with skyrmions. The desirable pattern is programmed using the MFM control software. The flexibility and further development of this approach related to the topological modification of the environment will make it possible to obtain regions with a minimum size corresponding to the skyrmion lattice period, which is approximately 250 nm in our case. Future development of this technique could include making material stacks, where one can write skyrmions and monodomain areas instead of worm-like textures.

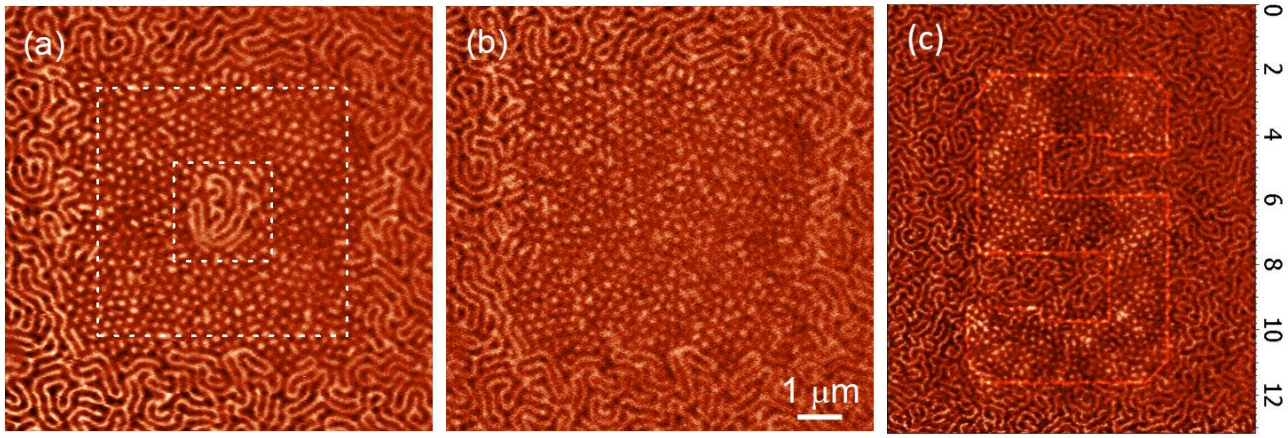

Figure 4. Zero-field MFM images of the domain structure of the $(Pt/CoFeSiB/W)_{11}$ with the created area filled by skyrmions and with non-scanned central region (a). The outer and inner borders indicated by white dashed lines delimit the scanning region in the tapping mode. The same area after full filling by skyrmions (b). Realization of S symbol by skyrmion nanolithography on the surface of the $(Pt/CoFeSiB/W)_{11}$ film (c). The MFM image size is $11 \times 13\ \mu m^2$. The red line delimits the tapping mode scanned area.

To characterize the generated skyrmion lattices, the MFM images were converted to grey scale to obtain the positions of the skyrmions with the Trackpy software package.[38] Based on these positions, two parameters that characterize the ordering in the lattice are calculated:[39] (i) the pair correlation function and (ii) local orientational order parameters. The one-dimensional pair correlation function *g(r)* shown in Fig. 5(a) gives the normalized skyrmion density distribution as a function of the distance between skyrmions. The first and the second peak indicate the preferred distances of the nearest and next-nearest neighbors, which are approximately 0.26 μm and 0.50 μm, respectively.

To characterize the state of the skyrmion lattice displayed in Fig. 4(b), the local orientational order parameter ψ_6 has been computed. This complex number is a standard parameter to quantify the emergence of local hexagonal order $|\psi_6| = 1$ for a perfect triangular lattice and decreases to 0

with the increasing disorder. It can be used to describe the state and monitor possible phase transitions of the system. For the snapshot presented in Fig. 5(b) the average value of $|\psi_6|$ (taken over all particles excluding the boundary region) is approximately 0.55. Fig. 5(b) displays the spatial distribution of $|\psi_6|$, which indicates that the local hexagonal order is relatively inhomogeneous. Fig. 5(c) displays the spatial distribution of θ (the Euler angle of ψ_6 divided by 6), which visualizes clusters of skyrmions with similar local orientation. Our quantitative analysis of the lattice state allows us to identify the phase as a dense two-dimensional liquid.[40]

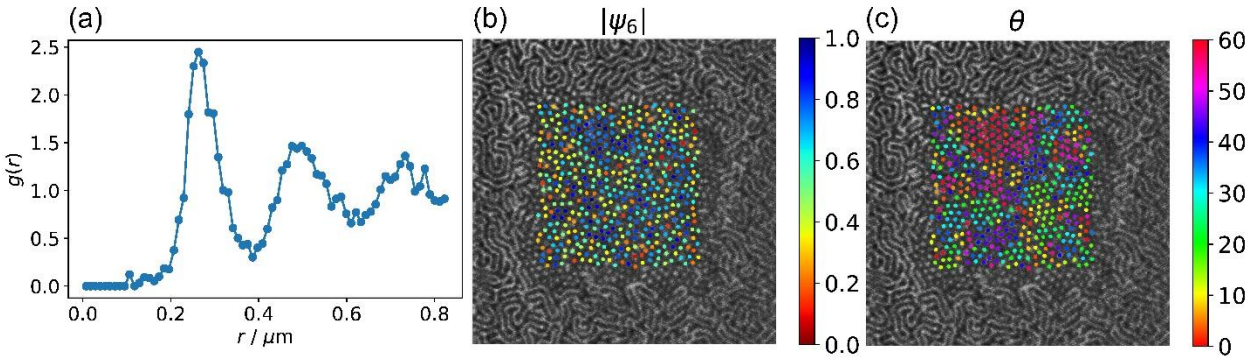

Figure 5. (a) One-dimensional pair correlation function *g(r)*. (b) Spatial distribution of $|\psi_6|$. (c) Spatial distribution of orientation angle θ.

Micromagnetic simulations

To understand the MFM tip-assisted skyrmion lattice nucleation process, micromagnetic simulations were performed, in which the multilayer structure $(Pt/CoFeSiB/W)_{11}$ was replaced with a single uniform ferromagnetic layer according to the effective medium approach.[18,41] The detailed description of the simulation procedure can be found in the Methods section. The magnetic parameters of the real structure and the effective model used in simulations are presented in Table 1.

TABLE 1. Parameters for micromagnetic simulations.

	Saturation magnetization	Exchange stiffness	Uniaxial anisotropy	Effective IDMI constant	Gilbert damping
	M_s (emu/cm^3)	A_{ex} (10^{-7} erg/cm)	K_u (10^6 erg/cm^3)	D_{eff} (erg/cm^2)	α
Real structure	950	12	7.27	−1.09	0.1
Effective model	408	5.15	1.74	−0.47	0.1

To confirm the adequacy of using the effective model, the simulated magnetization reversal process was compared with the experimental hysteresis loop and domain structure, as shown in Fig. 6. There are insignificant discrepancies at the saturation field: in simulations, the annihilation of 360° domain walls and complete saturation of a defect-free film occur in larger magnetic fields, in contrast to that in the experiment (H_{sat} =1500 Oe in simulation). Periods of the labyrinth domain structure from the MFM image and from the simulation are similar and equal to 250 nm, as shown in Figs. 6 (b, c).

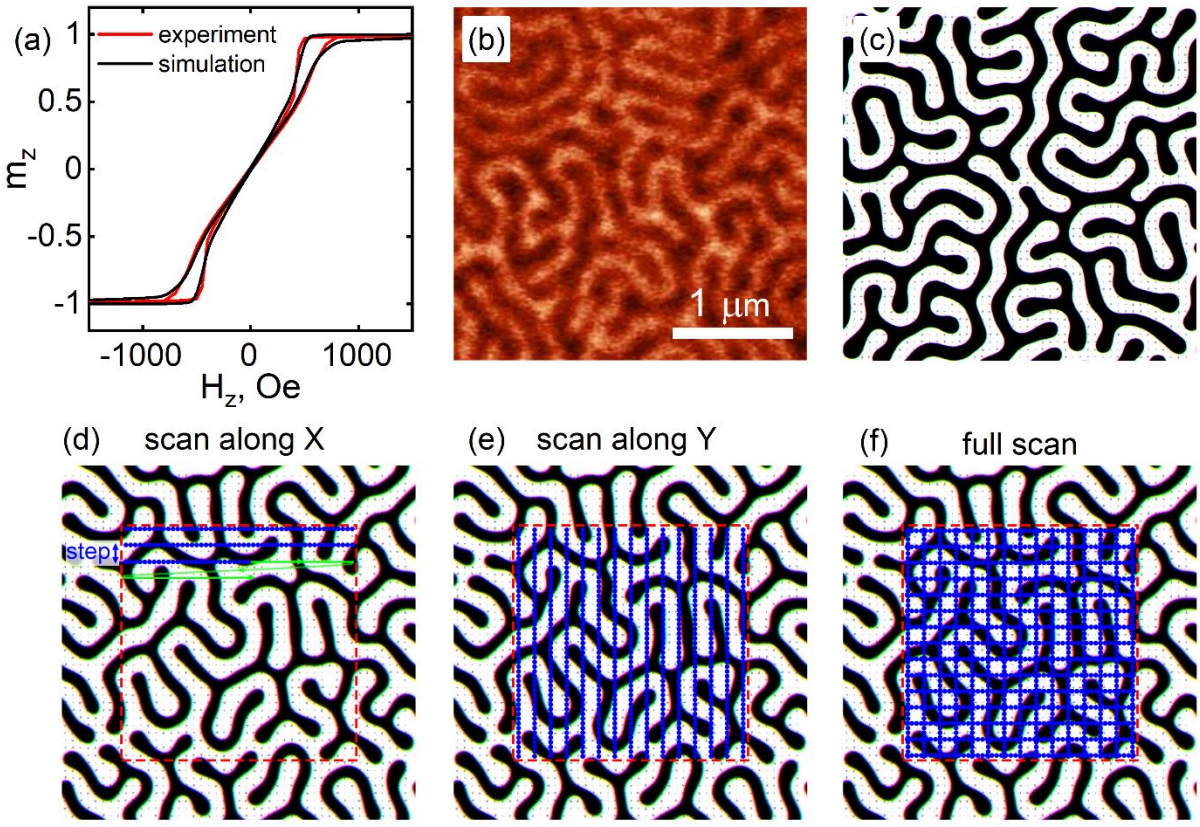

Figure 6. (a) Experimental and simulated out-of-plane hysteresis loops for the $(Pt/CoFeSiB/W)_{11}$ film. Domain structure at remanence captured by MFM (b) and generated by simulations (c). Schemes of the tip scanning trajectories in the micromagnetic simulations: (d) X direction, (e) Y direction, and (f) after the X and Y scans.

Simulations of the MFM tip stray field effects on the domain structure were performed using a magnetic field localized as a round spot with the step-like field profile (blue dots in Fig. 6(d)). Inside the modeling area, the central region of $2 \times 2\ \mu m^2$ (red dashed lines limit the scanning region in Figs. 6(d–f)) was scanned by these spots with a shift along the X and Y directions equal to the spot size, *i.e.*, the tip draws a continuous line. The trajectories of the tip movement are represented by the green line in Fig. 6(d). The experimental scanning step of 200 nm corresponds to the

distance between the adjacent lines. The probe passed the scanning area 5 times along the X (Fig. 6(d)) and Y (Fig. 6(e)**)** directions similar to that in the experiment.

In the experiment, during a scan in the tapping mode, a local field created by the magnetic tip was fixed (H_{tip}), and an additional external magnetic field (H_{ext}) was applied to assist the skyrmion nucleation. Therefore, the local magnetic field in the simulations was taken as a sum: $H_{local} = H_{tip} + H_{ext}$. The simulated scanning results strongly depend on the tip spot size and H_{local}. As discussed above, the labyrinth domains are converted into skyrmions by the magnetic tip when $H_{local} \approx H_{sat}$. To study the effect of the local field spot size on the efficiency of skyrmion nucleation, the probe scanning was simulated with $H_{local} > H_{sat}$, and the dependence of the skyrmion density (ρ) was plotted as a function of the spot size (Fig. S3(a) in the Supplementary file). The measured values of ρ were normalized to the maximum skyrmion density with hexagonal packaging ($\rho_{max} = \frac{2}{\sqrt{3}} a_{SkL}^{-2}$, where a_{SkL} is the skyrmion lattice constant).

The obtained results exhibit that even if $H_{local} > H_{sat}$, the spot size has to be sufficiently large (at least 100 nm, as seen in Fig. S3(a) in the Supplementary file) for skyrmion nucleation. This spot size is related to the width of a domain wall (DW). In our case, the calculated DW width is 40 nm (Fig. S3(b) in the Supplementary file); therefore, the spot size has to be twice as large as the DW width for effective skyrmion generation. Further simulations were conducted with the local field spot size 100 nm.

The following simulations allow to explore the effect of the local field magnitude. The full scanning process with $H_{local} \leq 0.5 H_{sat}$ is displayed in Supplementary Movie 1, and the final domain structure is presented in Fig. 7(a). Such a weak field is not sufficient for slicing the stripe domains into skyrmions. Only the labyrinth alignment is observed along X and Y directions. The positive local field becomes able to slice the stripe domains into separate skyrmions with negative polarity,

when H_{local} is comparable with H_{sat}. Figure 7(b) displays the final domain structure after scanning with $H_{local} = 0.7H_{sat}$. To create the skyrmion lattice with maximum density, H_{local} has to be higher than H_{sat}. Supplementary Movie 2 shows the process of nucleation of the skyrmion lattice at a high local field. The stabilized skyrmion lattice is displayed in Fig. 7(c). Figure 7(d) displays the dependence of $\rho/\rho_{max} = H_{local}/H_{sat}$ for the experimental and simulated data. The observed good agreement between the experiment and simulation allows to conclude that for the efficient nucleation of a skyrmion lattice, the local field size has to be twice higher than the DW width, and H_{local} has to be equal or above H_{sat}. An estimation of ground states from the simulations revealed that the formed skyrmion lattice does not have the lowest energy density ($E_{sk} = -1.206\times10^6$ erg/cm^3); however, the energy density is compatible with the total energy of the labyrinth structure ($E_{sk} = -1.203\times10^6$ erg/cm^3).

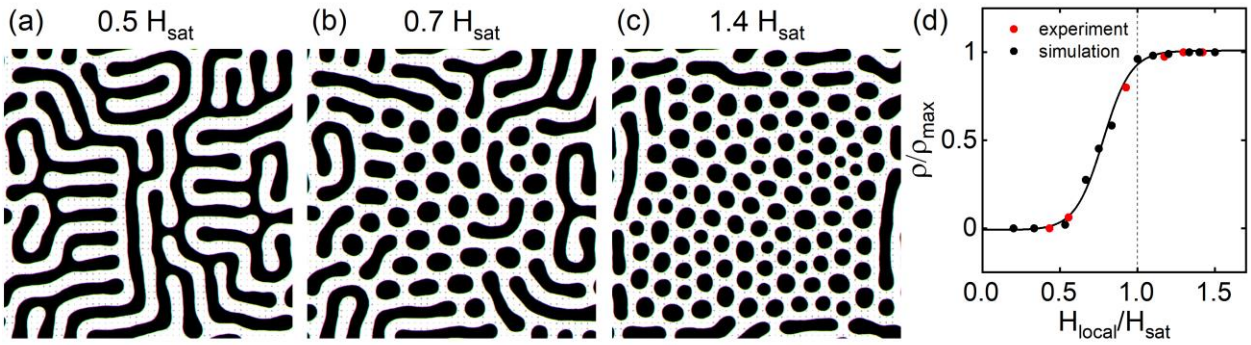

Figure 7 (a–c) Simulated domain structure of the $(Pt/CoFeSiB/W)_{11}$ film after the five-pass scanning with different local field values (H_{local}) expressed in units of the saturation field (H_{sat}). (d) Dependence of the normalized density of the skyrmions on the H_{local}/H_{sat} ratio.

Supplementary Movie 2 also displays that the number of nucleated skyrmions increases with the number of passes. When the skyrmion lattice fills the entire area of the scanning region, the skyrmions are expelled out of the exposed region. The formation of skyrmions behind the scanning

area was also observed in the experiment. Therefore, for the optimal nucleation of a skyrmion lattice inside a given region, it is necessary to not only regulate the magnitude of the local field but also to select the required number of scanning passes. The sequential change of the domain structure with the increasing number of passes is presented in Fig. S4 in the Supplementary file.

An optimization of the skyrmion lattice nucleation process is possible by a pre-ordering of the domain structure. Since the effective slicing of labyrinth domains into skyrmions occurs during the transverse motion of the MFM probe relative to the stripes, provided that the stripe domains are ordered along the X axis, then it will be sufficient to make scanning only along the Y direction. The ordered stripe domain structure could be quickly created after the in-plane saturation by an external magnetic field. Supplementary Movie 3 presents the demagnetisation process after saturation along the X direction. Then this relaxed stripe structure was scanned by a local magnetic field immediately along the Y direction (Fig. S5(a-c) in the Supplementary file). Since the field of the MFM probe was enough for the slicing of stripes (H_{local}=1.4H_{sat}), each interaction of the probe with an oppositely magnetized stripe domain led to the nucleation of a new skyrmion. Therefore, only one pass along the Y direction is sufficient to form a highly dense skyrmion lattice in the scanning region (Fig. S5(d) in the Supplementary file).

Figure 8(a) presents the dependence of the skyrmion lattice constant (a_{SkL}) as a function of IDMI strength for experimentally measured magnetic parameters. The values of a_{SkL} were determined by calculating the system energy density as a function of a_{SkL} (inset in Fig. 8(a)). The calculation details can be found in Methods section. In the calculation of the lattice constant, 11 layers with "real structure" parameters (Table 1) were considered. The magnetic layers were in contact, and the direct exchange interaction between them was set to zero. Two Bloch skyrmions were placed within the rectangular unit cell (Fig. 8(b)) as an initial condition, and the system was let to relax

to non-uniform skyrmion state over the thickness. The lattice constant was obtained from the calculation of the minimum energy density as a function of the computational unit cell size in x-direction, a_x. The minimum of this function corresponds to a_{SkL}, see the inset in Fig. 8(a). The lattice constant of 252 nm found for "real structure" parameters is close to that obtained in experiment (the peak in *g(r)* function is approximately at 260 nm, Fig.5(a)). The skyrmion diameter was about 186 nm. The small difference between the experimental and calculated values might be owing to the sample non-uniformities that can influence the stability of skyrmions in experimental samples.[42]

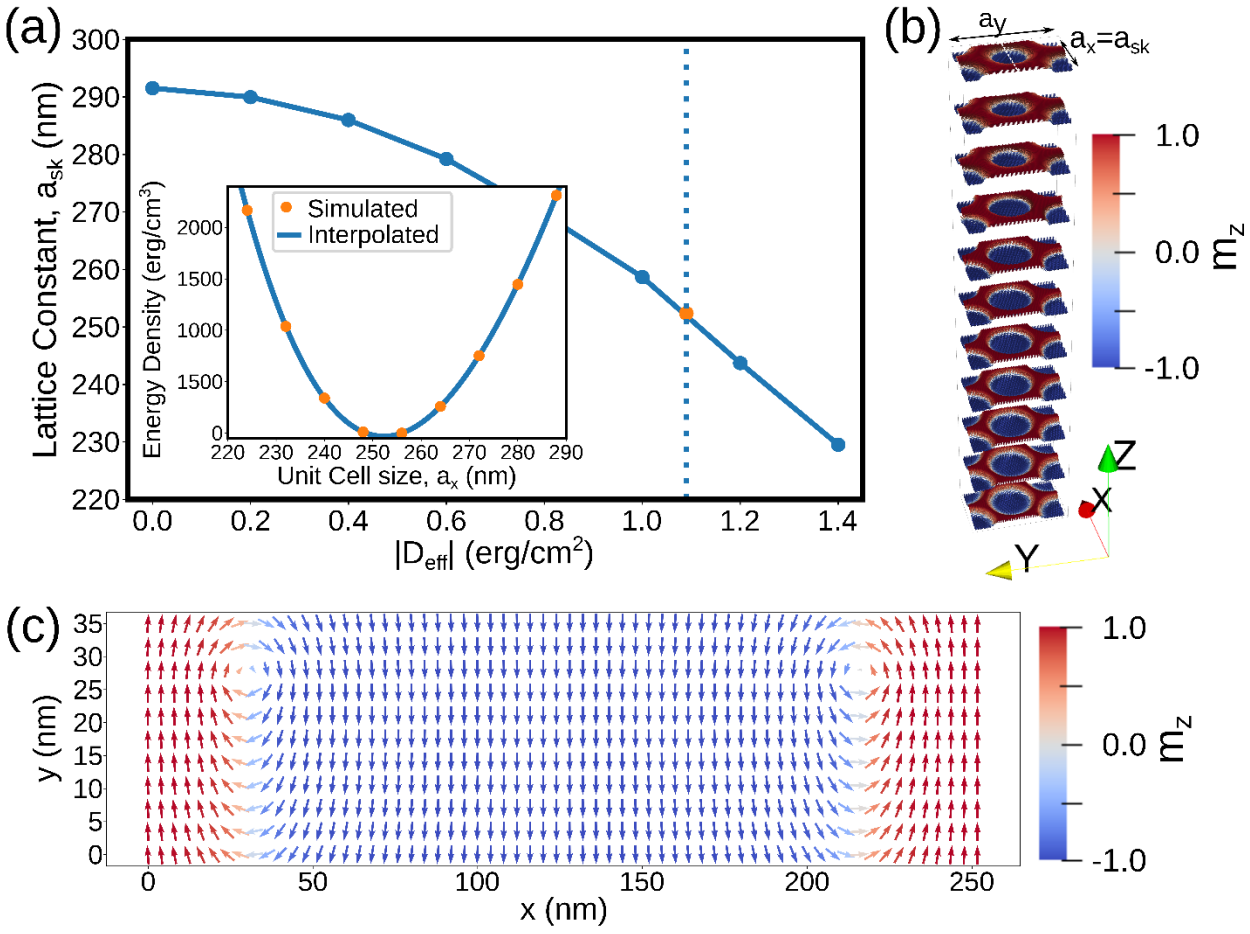

Figure 8 (a) Skyrmion lattice constant as a function of the IDMI strength. The vertical dashed line indicates the value of $D_{eff} = -1.09$ erg/cm^2 measured experimentally. The inset presents the method of calculation of the lattice constant for $D_{eff} = -1.09$ erg/cm^2, *i.e.*, minimization of the energy density as a function of the

lattice constant. (b) The hexagonal skyrmion lattice simulated by a centered rectangular unit cell for D_{eff} = −1.09 erg/cm^2. (c) The XZ-plane at the Y center of the unit cell with a color scale proportional to m_z magnetization component.

The stable configuration calculated for the experimentally determined set of parameters is presented in Figs. 8(b, c) consisting of eleven layers hosting skyrmions with different helicities. The top two and seven bottom layers possess opposite Néel-type chirality, whereas the third layer has Bloch-type chirality.[43] The origin of opposite Néel-type chiralities is due to the strong stray field arising near the bottom or top layers, between the two perpendicularly magnetizing domains, as in dipolarly stabilized magnetic bubbles.[44] The ratio 2:8 of different types of skyrmions is induced by the interplay of IDMI interaction and dipole interactions. One of Néel-type chiralities is preferred by IDMI interaction, whereas the dipole interaction favors an equal distribution of opposite chiralities.[45-48]

Conclusion

In this study, we technologically demonstrated the writing of arbitrary skyrmion ensembles and provided concrete parameters to achieve this with controllable and localized skyrmion nucleation by stray fields of MFM tips. By scanning the tip over certain areas, a technique of skyrmion nanolithography that allows the creation of local ordered ensembles of skyrmions in multilayered nanostructures or films with PMA and IDMI with the lateral resolution of 200 nm was developed. Besides the tip's lift height and an assisting external magnetic field, the scanning step (distance between two adjacent scanning lines) is a crucial parameter to control skyrmion lattice characteristics. Moreover, a variation of the scanning step allows one to decrease the number of scans resulting in the complete formation of the skyrmion lattice. The advantage of our approach

is that one can locally nucleate skyrmions that might be energetically metastable at an energy that is higher than that of the worm-like domain state. This cannot be achieved by other techniques like RF excitation and current-induced heating. Moreover, this technique is non-invasive for the materials used, in contrast to FIB-, EBL- and laser-assisted methods. Using the one-dimensional pair correlation function *g(r)* and the local orientational order parameter ψ_6, the fabricated skyrmion lattices have been characterized as a dense two-dimensional liquid with short-range correlations.

Our approach offers possibilities for developing basic elements of non-conventional logic and neuromorphic spintronics, creating environments for the realization of skyrmion racetrack memory, and studying the interface-induced phenomena such as topological Hall effect. The alignment of skyrmions into ordered geometric regions will allow the fabrication of magnonic crystals based on skyrmions and assign trajectories of complex shapes for the propagation of spin waves in a skyrmion lattice. Another promising aspect of using skyrmion (topological) nanolithography is the possibility of studying the interaction of skyrmions with a labyrinth domain structure and the features of the dynamic properties of skyrmions and chiral domain walls.

Methods

The series of samples based on a Ta(3)/Pt(7)/[P(1)/CoFeSiB(1.5)/W(1)]$_n$/Ta(5) structure with the number of stacks n = 1, 3, 5, 11, 21 were sputter-deposited onto 1.25 × 1.25 cm^2 thermally oxidized Si wafers under a base pressure below 5 × 10^{-9} Torr. The thickness of the SiO_2 oxide layer was 300 nm.

To study the magnetic microstructure of the multilayer films, a (Pt/CoFeSiB/W)$_{11}$ structure was deposited onto an optically transparent 100-nm thick Si_3N_4 membrane. The domain structure was

imaged in a full-field magnetic transmission soft X-ray microscope (MTXM), XM-1, at the beamline 6.1.2 at the Advanced Light Source (Center for X-Ray Optics, Lawrence Berkeley National Laboratory, USA).

To study the magnetic structure by MFM (Ntegra Aura NT-MDT), a two-pass technique was used. All scans were performed using magnetic probes. At the first pass, the surface topology was probed using the "tapping mode." In this mode, the distance between the sample surface and the tip apex was less than 10 nm (in theory near 1 nm). At the second pass, when the magnetic probe was raised to an approximate height of 50 nm, the domain structure was scanned by subtracting the inclination of the sample plane ("non-contact" mode). In the case of the tapping mode, the magneto-static interaction between the probe and the sample is much larger than in the non-contact mode. Therefore, the change in the magnetic structure of the samples under the action of stray fields is possible, which must be considered.[26,27] As for the magnetic probes, standard ASYMFM-R2 tips (Asylum Research) with the radius of 47 ± 5 nm and a 50-nm-thick CoCr magnetic coating were used.

To understand the MFM tip-assisted skyrmion lattice nucleation process, micromagnetic simulations with the Mumax^3 software package[49] were performed. The multilayer structure $(Pt/CoFeSiB/W)_{11}$ was replaced with a single uniform ferromagnetic layer according to the effective medium approach.[18,41] Effective modeling parameters for the film were calculated correspondingly for the ratio $k = t_r/t_m = 2.33$, where $t_r = 3.5$ nm is the thickness of one stack, and $t_m = 1.5$ nm is the thickness of the magnetic layer. The magnetic parameters utilized in the simulations are presented in Table 1. The total thickness of the single ferromagnetic layer was $t_{FM} = 11t_r = 38.5$ nm. The modeling area of the film was 3×3 μm^2 with cell size $4 \times 4 \times t_{FM}$ nm^3. The periodic boundary conditions were set on edges of the modeling area. The thermal field effect was

considered in all simulations with a room temperature of 300 K. Simulations of the hysteresis processes were started from a monodomain state with two bubble domains. These point domains with the size of 20 nm act as nucleation centers for the growing labyrinth domain structure.

To simulate the lattice constant a_{SkL}, the "real structure" parameters (Table 1) were used. The centered rectangular unit cell and periodic boundary conditions were employed to describe a hexagonal skyrmion lattice, see Fig. 8(b). The hexagonal lattice can be viewed as a special case of a centered rectangular lattice when $\frac{a_y}{a_x} = \sqrt{3}$, as it is in our calculations. The size of the unit cell was defined by the number of the computational cells, N_x, N_y=2N_x, N_z= 73, and cell sizes, c_x, c_y, c_z. N_z and c_z were fixed to N_z = 73 and c_z = 0.5 nm to simulate 11 magnetic layers of 1.5 nm thickness separated by 2-nm-thick non-magnetic spacer. The c_x and c_y were fixed to: c_x=2 nm, $c_y = \sqrt{3}$ nm. N_x and N_y parameters were varied to impose different lattice constants of a skyrmion lattice and calculate the energy density as a function of the computational unit cell size. The minimum of this function corresponds to a_{SkL}, see the inset in Fig. 8 (a). Two skyrmions with Bloch-type chirality were placed within the rectangular unit cell as an initial state before relaxation of the system. This initial state allows the relaxation algorithm to stabilize to the final state of a nonuniform skyrmion (with opposite Néel-type chiralities near the top and bottom edges) for any value of IDMI (any ratio of Néel-type chiralities in layers).

ASSOCIATED CONTENT

Supporting Information

Supporting Information is available free of charge at

Figures S1 to S5: Magnetic hysteresis loops measured in OOP and IP geometries for samples with different number of stack's repetition; Surface topology and domain structure of the sample with n=11; Dependence of the normalized density of skyrmions on the local magnetic field spot size and micromagnetic profile of a domain wall; Simulation of skyrmion lattice nucleation by means of a local magnetic field with increasing number of scanning passes; The algorithm of optimized skyrmion lattice nucleation process.

Movies 1 to 3: The simulated scanning process by the MFM tip with $H_{local} \leq 0.5H_{sat}$; The simulated process of nucleation of the skyrmion lattice at a high local field; Simulation results of one pass scanning along the Y direction to form a highly dense skyrmion lattice from the stripe domain structure realized after demagnetization.

AUTHOR INFORMATION

Corresponding Authors

*E-mail: ykim97@korea.ac.kr

**E-mail: samardak.as@dvfu.ru

ORCID

Alexey Ognev 0000-0002-1619-3666

Alexander Kolesnikov 0000-0001-9715-7212

Alexandr Sadovnikov 0000-0002-8847-2621

Ivan Soldatov 0000-0002-2911-1842

Mathias Kläui 0000-0002-4848-2569

Young Keun Kim 0000-0002-0868-4625

Alexander Samardak 0000-0001-5917-4361

Complete contact information is available at:

Author Contributions

A.V.O., A.S.S., and Y.K.K. elaborated the research idea and proposed samples and experiments. Y.J.K. and I.H.C. prepared the experimental samples and measured the magnetic properties. O.A.V., A.T., and J.M. conducted the MFM study. A.V.S. and S.A.N. probed the samples by BLS. I.V.S. and A.S.S. studied the magnetization reversal and domain structure by Kerr microscopy. A.G.K. and M.M. performed the micromagnetic simulations. Y.G., N.K., F.D., P.V., and M.K. analyzed the topological order of skyrmions. A.S.S., A.V.O., and Y.K.K. wrote the majority of the manuscript with input from all co-authors. A.S.S. and Y.K.K. supervised the research implementation.

Notes

The authors declare no competing financial interest.

Acknowledgements

This work is supported by the Russian Foundation for Basic Research (grant 17-52-45135) and INT/RUS/RFBR/P-273 grant, the Russian Ministry of Education and Science under the state task (0657-2020-0013) and the program of improvement of the competitiveness of Far Eastern Federal University (Agreement № 075-02-2020-1584), by Act 211 of the Government of the Russian Federation (contract No. 02.A03.21.0011). This work was partially supported by Era.Net RUS Plus (TSMFA), RFBR (project no. 18-29-27026, 18-57-76001) and the scholarship of President of the Russian Federation for young scientists and graduate students (SP-350.2019.1). A.S. Samardak thanks the DAAD and the Russian Ministry of Education and Science (Agreement № 075-03-2020-188/6) for funding a research stay at Johannes Gutenberg University Mainz. The group in Mainz thanks the German Research Foundation (SPP2137 #403502522 and SFB TRR173 #268565370). This research was also supported by the National Research Foundation of Korea (2015M3D1A1070465, 2020M3F3A2A01082591), and in part by the University R&D program of Samsung Electronics. M. Mruczkiewicz acknowledges ITMS project code 313021T081.

Conflict of Interest

The authors declare no conflict of interest.

References

1. Fert, A.; Reyren, N.; Cros, V. Magnetic Skyrmions: Advances in Physics and Potential Applications. *Nature Reviews Materials* 2017, 2, 17031.

2. Jiang, W.; Chen, G.; Liu, K.; Zang, J.; Te Velthuis, S. G. E.; Hoffmann, A. Skyrmions in Magnetic Multilayers. *Physics Reports* 2017, 704, 1–49.

3. Je, S.-G.; Han, H.-S.; Kim, S.K.; Montoya, S.A.; Chao, W.; Hong, I.-S.; Fullerton, E.E.; Lee, K.-S.; Lee, K.-J.; Im, M.-Y.; Hong, J.-I. Direct Demonstration of Topological Stability of Magnetic Skyrmions *via* Topology Manipulation. *ACS Nano* 2020, 14, (3), 3251-3258.

4. Bogdanov, A. N.; Panagopoulos, C. The Emergence of Magnetic Skyrmions. *Physics Today* 2020, 73, (3), 44–49.

5. Rózsa, L.; Deák, A.; Simon, E.; Yanes, R.; Udvardi, L.; Szunyogh, L.; Nowak, U. Skyrmions with Attractive Interactions in an Ultrathin Magnetic Film. *Physical Review Letters* 2016, 117, (15), 157205.

6. Bläsing, R.; Khan, A. A.; Filippou, P. C.; Garg, C.; Hameed, F.; Castrillon, J.; Parkin, S. S. P. Magnetic Racetrack Memory: From Physics to the Cusp of Applications within a Decade. *Proceedings of the IEEE* 2020, 1–19.

7. Yu, G.; Upadhyaya, P.; Shao, Q.; Wu, H.; Yin, G.; Li, X.; He, C.; Jiang, W.; Han, X.; Amiri, P. K.; Wang, K. L. Room-Temperature Skyrmion Shift Device for Memory Application. *Nano Letters* 2017, 17, (1), 261–268.

8. Luo, S.; Song, M.; Li, X.; Zhang, Y.; Hong, J.; Yang, X.; Zou, X.; Xu, N.; You, L. Reconfigurable Skyrmion Logic Gates. *Nano Letters* 2018, 18, (2), 1180–1184.

9. Everschor-Sitte, K.; Masell, J.; Reeve, R. M.; Kläui, M. Perspective: Magnetic Skyrmions—Overview of Recent Progress in an Active Research Field. *Journal of Applied Physics* 2018, 124, (24), 240901.

10. Grollier, J.; Querlioz, D.; Camsari, K. Y.; Everschor-Sitte, K.; Fukami, S.; Stiles, M. D. Neuromorphic Spintronics. *Nature Electronics* 2020.

11. Moreau-Luchaire, C.; Moutafis, C.; Reyren, N.; Sampaio, J.; Vaz, C. A. F.; Van Horne, N.; Bouzehouane, K.; Garcia, K.; Deranlot, C.; Warnicke, P.; Wohlhüter, P.; George, J. M.; Weigand, M.; Raabe, J.; Cros, V.; Fert, A. Additive Interfacial Chiral Interaction in Multilayers for Stabilization of Small Individual Skyrmions at Room Temperature. *Nature Nanotechnology* 2016, 11, 444.

12. Soumyanarayanan, A.; Raju, M.; Gonzalez Oyarce, A. L.; Tan, A. K. C.; Im, M.-Y.; Petrović, A. P.; Ho, P.; Khoo, K. H.; Tran, M.; Gan, C. K.; Ernult, F.; Panagopoulos, C. Tunable Room-Temperature Magnetic Skyrmions in Ir/Fe/Co/Pt Multilayers. *Nature Materials* 2017, 16, (9), 898–904.

13. Samardak, A.; Kolesnikov, A.; Stebliy, M.; Chebotkevich, L.; Sadovnikov, A.; Nikitov, S.; Talapatra, A.; Mohanty, J.; Ognev, A. Enhanced Interfacial Dzyaloshinskii-Moriya Interaction and Isolated Skyrmions in the Inversion-Symmetry-Broken Ru/Co/W/Ru Films. *Applied Physics Letters* 2018, 112, (19), 192406.

14. Lin, T.; Liu, H.; Poellath, S.; Zhang, Y.; Ji, B.; Lei, N.; Yun, J. J.; Xi, L.; Yang, D. Z.; Xing, T.; Wang, Z. L.; Sun, L.; Wu, Y. Z.; Yin, L. F.; Wang, W. B.; Shen, J.; Zweck, J.; Back, C. H.; Zhang, Y. G.; Zhao, W. S. Observation of Room-Temperature Magnetic Skyrmions in Pt/Co/W Structures with a Large Spin-Orbit Coupling. *Physical Review B* 2018, 98, (17), 174425.

15. Soldatov, I. V.; Jiang, W.; Te Velthuis, S. G. E.; Hoffmann, A.; Schäfer, R. Size Analysis of Sub-Resolution Objects by Kerr Microscopy. *Applied Physics Letters* 2018, 112, (26), 262404.

16. Nandy, A. K.; Kiselev, N. S.; Blügel, S. Interlayer Exchange Coupling: A General Scheme Turning Chiral Magnets into Magnetic Multilayers Carrying Atomic-Scale Skyrmions. *Physical Review Letters* 2016, 116, (17), 177202.

17. Kang, S. P.; Kim, N. J.; Kwon, H. Y.; Choi, J. W.; Min, B. C.; Won, C. The Spin Structures of Interlayer Coupled Magnetic Films with Opposite Chirality. *Scientific Reports* 2018, 8, (1), 2361.

18. Woo, S.; Litzius, K.; Krüger, B.; Im, M.-Y.; Caretta, L.; Richter, K.; Mann, M.; Krone, A.; Reeve, R. M.; Weigand, M.; Agrawal, P.; Lemesh, I.; Mawass, M.-A.; Fischer, P.; Kläui, M.; Beach, G. S. D. Observation of Room-Temperature Magnetic Skyrmions and Their Current-Driven Dynamics in Ultrathin Metallic Ferromagnets. *Nature Materials* 2016, 15, 501.

19. Litzius, K.; Lemesh, I.; Krüger, B.; Bassirian, P.; Caretta, L.; Richter, K.; Büttner, F.; Sato, K.; Tretiakov, O. A.; Förster, J.; Reeve, R. M.; Weigand, M.; Bykova, I.; Stoll, H.; Schütz, G.; Beach, G. S. D.; Kläui, M. Skyrmion Hall Effect Revealed by Direct Time-Resolved X-Ray Microscopy. *Nature Physics* 2017, 13, (2), 170–175.

20. Montoya, S. A.; Couture, S.; Chess, J. J.; Lee, J. C. T.; Kent, N.; Henze, D.; Sinha, S. K.; Im, M. Y.; Kevan, S. D.; Fischer, P.; Mcmorran, B. J.; Lomakin, V.; Roy, S.; Fullerton, E. E. Tailoring Magnetic Energies to Form Dipole Skyrmions and Skyrmion Lattices. *Physical Review B* 2017, 95, (2), 024415.

21. Desautels, R. D.; Debeer-Schmitt, L.; Montoya, S. A.; Borchers, J. A.; Je, S.-G.; Tang, N.; Im, M.-Y.; Fitzsimmons, M. R.; Fullerton, E. E.; Gilbert, D. A. Realization of Ordered Magnetic Skyrmions in Thin Films at Ambient Conditions. *Physical Review Materials* 2019, 3, (10), 104406.

22. Woo, S.; Song, K. M.; Zhang, X.; Zhou, Y.; Ezawa, M.; Liu, X.; Finizio, S.; Raabe, J.; Lee, N. J.; Kim, S.-I.; Park, S.-Y.; Kim, Y.; Kim, J.-Y.; Lee, D.; Lee, O.; Choi, J. W.; Min, B.-C.; Koo, H. C.; Chang, J. Current-Driven Dynamics and Inhibition of the Skyrmion Hall Effect of Ferrimagnetic Skyrmions in GdFeCo Films. *Nature Communications* 2018, 9, (1), 959.

23. Lee, J. C. T.; Chess, J. J.; Montoya, S. A.; Shi, X.; Tamura, N.; Mishra, S. K.; Fischer, P.; Mcmorran, B. J.; Sinha, S. K.; Fullerton, E. E.; Kevan, S. D.; Roy, S. Synthesizing Skyrmion Bound Pairs in Fe-Gd Thin Films. *Applied Physics Letters* 2016, 109, (2), 022402.

24. Zhang, S.; Zhang, J.; Zhang, Q.; Barton, C.; Neu, V.; Zhao, Y.; Hou, Z.; Wen, Y.; Gong, C.; Kazakova, O.; Wang, W.; Peng, Y.; Garanin, D. A.; Chudnovsky, E. M.; Zhang, X. Direct Writing of Room Temperature and Zero Field Skyrmion Lattices by a Scanning Local Magnetic Field. *Applied Physics Letters* 2018, 112, (13), 132405.

25. Garanin, D. A.; Capic, D.; Zhang, S.; Zhang, X.; Chudnovsky, E. M. Writing Skyrmions with a Magnetic Dipole. *Journal of Applied Physics* 2018, 124, (11), 113901.

26. Temiryazev, A. G.; Temiryazeva, M. P.; Zdoroveyshchev, A. V.; Vikhrova, O. V.; Dorokhin, M. V.; Demina, P. B.; Kudrin, A. V. Formation of a Domain Structure in Multilayer Copt Films by Magnetic Probe of an Atomic Force Microscope. *Physics of the Solid State* 2018, 60, (11), 2200–2206.

27. Casiraghi, A.; Corte-León, H.; Vafaee, M.; Garcia-Sanchez, F.; Durin, G.; Pasquale, M.; Jakob, G.; Kläui, M.; Kazakova, O. Individual Skyrmion Manipulation by Local Magnetic Field Gradients. *Communications Physics* 2019, 2, (1), 145.

28. Kazakova, O.; Puttock, R.; Barton, C.; Corte-León, H.; Jaafar, M.; Neu, V.; Asenjo, A. Frontiers of Magnetic Force Microscopy. *Journal of Applied Physics* 2019, 125, (6), 060901.

29. Schott, M.; Bernand-Mantel, A.; Ranno, L.; Pizzini, S.; Vogel, J.; Béa, H.; Baraduc, C.; Auffret, S.; Gaudin, G.; Givord, D. The Skyrmion Switch: Turning Magnetic Skyrmion Bubbles on and off with an Electric Field. *Nano Letters* 2017, 17, (5), 3006–3012.

30. Je, S.-G.; Vallobra, P.; Srivastava, T.; Rojas–Sánchez, J.-C.; Pham, T. H.; Hehn, M.; Malinowski, G.; Baraduc, C.; Auffret, S.; Gaudin, G.; Mangin, S.; Béa, H.; Boulle, O. Creation of Magnetic Skyrmion Bubble Lattices by Ultrafast Laser in Ultrathin Films. *Nano Letters* 2018, 18, (11), 7362–7371.

31. Guang, Y.; Peng, Y.; Yan, Z; Liu, Y.; Zhang, J.; Zeng, X.; Zhang, S.; Zhang, S.; Burn, D. M.; Jaouen, N.; Wei, J.; Xu, H.; Feng, J.; Fang, C.; Van Der Laan, G.; Hesjedal, T.; Cui, B.; Zhang, X.; Yu, G.; Han, X. Electron Beam Lithography of Magnetic Skyrmions. *Advanced Materials* 2020, 32, 2003003.

32. Lemesh, I.; Litzius, K.; Böttcher, M.; Bassirian, P.; Kerber, N.; Heinze, D.; Zázvorka, J.; Büttner, F.; Caretta, L.; Mann, M.; Weigand, M.; Finizio, S.; Raabe, J.; Im, M.-Y.; Stoll, H.; Schütz, G.; Dupé, B.; Kläui, M.; Beach, G. S. D. Current-Induced Skyrmion Generation through Morphological Thermal Transitions in Chiral Ferromagnetic Heterostructures. *Advanced Materials* 2018, 30, (49), 1805461.

33. Li, W.; Bykova, I.; Zhang, S.; Yu, G.; Tomasello, R.; Carpentieri, M.; Liu, Y.; Guang, Y.; Gräfe, J.; Weigand, M.; Burn, D. M.; Van Der Laan, G.; Hesjedal, T.; Yan, Z.; Feng, J.; Wan, C.; Wei, J.; Wang, X.; Zhang, X.; Xu, H. *et al*. Anatomy of Skyrmionic Textures in Magnetic Multilayers. *Advanced Materials* 2019, 31, (14), 1807683.

34. Prychynenko, D.; Sitte, M.; Litzius, K.; Krüger, B.; Bourianoff, G.; Kläui, M.; Sinova, J.; Everschor-Sitte, K. Magnetic Skyrmion as a Nonlinear Resistive Element: A Potential Building Block for Reservoir Computing. *Physical Review Applied* 2018, 9, (1), 014034.

35. Allwood, D. A.; Schrefl, T.; Hrkac, G.; Hughes, I. G.; Adams, C. S. Mobile Atom Traps Using Magnetic Nanowires. *Applied Physics Letters* 2006, 89, (1), 014102.

36. Garst, M.; Waizner, J.; Grundler, D. Collective Spin Excitations of Helices and Magnetic Skyrmions: Review and Perspectives of Magnonics in Non-Centrosymmetric Magnets. *Journal of Physics D: Applied Physics* 2017, 50, (29), 293002.

37. Ma, F.; Zhou, Y.; Braun, H. B.; Lew, W. S. Skyrmion-Based Dynamic Magnonic Crystal. *Nano Letters* 2015, 15, (6), 4029–4036.

38. van der Wel, C.; Allan, D.; Keim, N.; Caswell, Th. *Trackpy*, 0.4.2; Trackpy Contributors: USA, 2019.

39. Zázvorka, J.; Dittrich, F.; Ge, Y.; Kerber, N.; Raab, K.; Winkler, Th.; Litzius, K.; Veis, M.; Virnau, P.; Kläui, M. Skyrmion Lattice Phases in Thin Film Multilayer. *Adv. Funct. Mater.* 2020, 2004037.

40. Nishikawa, Y.; Hukushima, K.; Krauth, W. Solid-Liquid Transition of Skyrmions in a Two-Dimensional Chiral Magnet. *Physical Review B* 2019, 99, (6), 064435.

41. Shigeo, H.; Yukinori, I.; Tetsuzo, K. Magnetostatic Energy and Magnetization Process in Multilayers with Perpendicular Anisotropy. *Journal of Magnetism and Magnetic Materials* 1992, 111, (3), 273–292.

42. Zeissler, K.; Mruczkiewicz, M.; Finizio, S.; Raabe, J.; Shepley, P. M.; Sadovnikov, A. V.; Nikitov, S. A.; Fallon, K.; Mcfadzean, S.; Mcvitie, S.; Moore, T. A.; Burnell, G.; Marrows, C. H. Pinning and Hysteresis in the Field Dependent Diameter Evolution of Skyrmions in Pt/Co/Ir Superlattice Stacks. *Scientific Reports* 2017, 7, (1), 15125.

43. Nagaosa, N.; Tokura, Y. Topological Properties and Dynamics of Magnetic Skyrmions. *Nature Nanotechnology* 2013, 8, (12), 899-911.

44. Alex Hubert, R. S., *Magnetic Domains: The Analysis of Magnetic Microstructures*. Springer Verlag Berlin Heidelberg: 2008; P 696.

45. Hrabec, A.; Sampaio, J.; Belmeguenai, M.; Gross, I.; Weil, R.; Chérif, S. M.; Stashkevich, A.; Jacques, V.; Thiaville, A.; Rohart, S. Current-Induced Skyrmion Generation and Dynamics in Symmetric Bilayers. *Nature Communications* 2017, 8, (1), 15765.

46. Chauleau, J.-Y.; Legrand, W.; Reyren, N.; Maccariello, D.; Collin, S.; Popescu, H.; Bouzehouane, K.; Cros, V.; Jaouen, N.; Fert A. Chirality in Magnetic Multilayers Probed by the Symmetry and the Amplitude of Dichroism in X-Ray Resonant Magnetic Scattering. *Physical Review Letters* 2018, 120, (3), 037202.

47. Legrand, W.; Chauleau, J.-Y.; Maccariello, D.; Reyren, N.; Collin, S.; Bouzehouane, K.; Jaouen, N.; Cros, V.; Fert A. Hybrid Chiral Domain Walls and Skyrmions in Magnetic Multilayers. *Science Advances* 2018, 4, (7), eaat0415.

48. Dovzhenko, Y.; Casola, F.; Schlotter, S.; Zhou, T. X.; Büttner, F.; Walsworth, R. L.; Beach, G. S. D.; Yacoby, A. Magnetostatic Twists in Room-Temperature Skyrmions Explored by Nitrogen-Vacancy Center Spin Texture Reconstruction. *Nature Communications* 2018, 9, (1), 2712.

49. Vansteenkiste, A.; Leliaert, J.; Dvornik, M.; Helsen, M.; Garcia-Sanchez, F.; Van Waeyenberge, B. The Design and Verification of Mumax3. *AIP Advances* 2014, 4, (10), 107133.